AGU ADVANCING EARTH AND SPACE SCIENCES

JGR Space Physics

RESEARCH ARTICLE
10.1029/2024JA033462

Special Collection:
Space Weather Events of 2024 May 9-15

The Magnetic Topology of AR13664 Leading to Its First Halo CME

D. MacTaggart[1], T. Williams[2], and O. P. M. Aslam[1]

[1]School of Mathematics and Statistics, University of Glasgow, Glasgow, UK, [2]Department of Mathematical Sciences, Durham University, Durham, UK

Abstract In the first half of May 2024, the solar active region (AR) NOAA 13664 was responsible for generating the strongest geomagnetic storm in over 20 years through an enhanced production of coronal mass ejections (CMEs). A key factor in this production was the complex magnetic topology of AR13664. In this work, we investigate the region's magnetic topology related to the production of its first halo CME on May 8th. This is achieved by combining different observations of magnetic topology based on photospheric magnetic helicity and winding signatures and nonlinear force-free field extrapolations, together with Atmospheric Imaging Assembly observations at different wavelengths. We present evidence that the first halo CME, and its associated X1.0 flare, was created by an emerging twisted flux tube within AR13664, following the general picture of the standard flare model. The coincidence of the first large magnetic winding signature with the start time of the X1.0 flare provides the onset time for the CME as well as the period of enhanced eruptive activity of the region—04:36 UT on May 8th.

Plain Language Summary The aurorae during May 2024, visible at many locations on the Earth, were caused by solar eruptions interacting with the Earth's magnetic field. Many of these eruptions originated from the same localized region of strong magnetic field in the solar atmosphere, referred to as active region (AR) 13664. An important part of how this region produced so many strong eruptions during a brief period lay in the complexity of its magnetic field, described as its *magnetic topology*. In this work, we study the magnetic topology of AR13664 in order to determine the magnetic configuration that led to the first large eruption directed toward the Earth, called a halo coronal mass ejection (CME). We provide evidence that this CME was created by a sub-region of twisted magnetic field that had emerged into the solar atmosphere. Our study also provides an effective start time for the enhanced eruption phase of AR13664—04:36 UT on May 8th.

Key Points:

- An observational investigation of the magnetic topology of AR13664 at the start of its phase of enhanced eruptivity
- Evidence to support that the emergence of pre-twisted magnetic field was responsible for the first halo coronal mass ejection (CME) of AR13664
- Photospheric signatures of the first halo CME of AR13664

Supporting Information:

Supporting Information may be found in the online version of this article.

Correspondence to:

D. MacTaggart,
david.mactaggart@glasgow.ac.uk

Citation:

MacTaggart, D., Williams, T., & Aslam, O. P. M. (2025). The magnetic topology of AR13664 leading to its first halo CME. *Journal of Geophysical Research: Space Physics*, *130*, e2024JA033462. https://doi.org/10.1029/2024JA033462

Received 21 OCT 2024
Accepted 4 APR 2025

Author Contributions:

Conceptualization: D. MacTaggart
Formal analysis: D. MacTaggart, O. P. M. Aslam
Funding acquisition: D. MacTaggart
Investigation: D. MacTaggart, T. Williams
Methodology: D. MacTaggart
Software: D. MacTaggart
Supervision: D. MacTaggart
Visualization: D. MacTaggart, T. Williams
Writing – original draft: D. MacTaggart
Writing – review & editing: D. MacTaggart, T. Williams, O. P. M. Aslam

1. Introduction

In May 2024, the aurorae that were visible across an extensive range of latitudes owed their origin to an enhanced period of coronal mass ejection (CME) activity. One of the main progenitors of this activity was the solar active region (AR) NOAA 13664. With the largest geomagnetic storm in over 20 years, registering a minimum Dst of −412 nT on May 11th, being traced to the activity of this region, it is natural that AR13664 has become a topic of intense study. In particular, the origin of its eruptive behavior is of interest, not only as a fundamental area of solar physics, but also in connection with the possibility of forecasting such intense activity in the future. In order to understand the onset of this eruptive activity, it is necessary to understand the behavior of the magnetic field of AR13664. Romano et al. (2024) has performed an analysis of the magnetic field at the photosphere using vector magnetograms from the Helioseismic and Magnetic Imager (HMI; Hoeksema et al., 2014) on board the Solar Dynamics Observatory (SDO; Pesnell et al., 2012). They investigate the period from May 2nd to May 11th and, based on magnetic data combined with velocity maps using the Differential Affine Velocity Estimator for Vector Magnetograms (DAVE4VM; Schuck, 2008), divide the evolution of AR13664 into key phases: the *early phase* (2nd–5th), the *emergence phase* (5th–7th), the *compaction phase* (7th–8th) and the *shearing phase* (8th–11th). This study reveals that AR13664 is characterized by several phases of complex dynamical activity, from the emergence of magnetic flux into a pre-existing region to the large-scale deformation of the AR. Some of the consequences in the solar atmosphere of the complex magnetic behavior observed in the photosphere has been studied by Jarolim et al. (2024). Using the SDO/HMI vector magnetograms, they produce a series of nonlinear force-free field (NLFFF) extrapolations to study the changes in magnetic energy and topology throughout the period of May 5th to May 11th, and find an excellent match between the occurrence of strong flares with dips in the free energy of their model. In a particular study of the magnetic field related to the X3.9 flare on May 10th, they reveal the detailed magnetic topology associated with this event. Kontogiannis (2024) studies the evolution of non-neutralized currents in AR13664, describing how these currents evolve in relation to the flux emergence events within AR13664 and the later evolution of the entire AR. Further, Kontogiannis (2024) shows that the magnitude of the total non-neutralized current far exceeds that of recent flare-intensive active regions.

All of the aforementioned works describe elements of the complexity of AR13664 throughout the period of its eruptivity. Due to the large number of eruptions deriving from it, AR13664 may be referred to as a *super active region* (Bai, 1988; Jaswal et al., 2025). This aspect, combined with the impact of these eruptions for the Earth, makes the detailed study of AR13664 and other such regions of great importance. The aim of this work is to complement the above studies of AR13664, that examine the entire region throughout its eruptive phase, by focusing on a particular detail - the evolution of the magnetic field leading to the first halo CME, produced on May 8th. To achieve this we make use of SDO/HMI vector magnetograms, which, as in the other studies, form the basis of our information about the magnetic field of AR13664. Using these data, the magnetic field is studied through calculations of magnetic helicity and winding fluxes in combination with NLFFF extrapolations. While the fluxes provide information about changes in magnetic topology at the photosphere, the extrapolations provide details of the three-dimensional (3D) magnetic structure and its connectivity in the corona. Together, these elements combine to give a detailed picture of the magnetic configuration leading to the first halo CME. Our thesis is that the observations point toward the eruptive phase of AR13664 being triggered by the emergence of a pre-twisted magnetic flux tube, a scenario that has been investigated in detail in many simulations (e.g., Hood et al., 2012; Patsourakos et al., 2020).

The rest of the paper proceeds as follows: first, we provide an overview of the approaches adopted to studying and interpreting magnetic topology signatures. We then present a detailed analysis of the magnetic topology of AR13664 before, during and after the eruption of the first halo CME, combining information from magnetic winding signatures and NLFFF extrapolations. The paper concludes with a brief summary and discussion.

2. Magnetic Topology

The importance of magnetic topology has long been recognized in solar physics (e.g., Longcope, 2005; Priest & Forbes, 2000). Before discussing the elements of magnetic topology used in this study, it is worthwhile to give a brief overview about what this term entails in the context of AR studies. The first important element of magnetic topology is that it describes the *connectivity* of magnetic field lines. Within an AR, there may be different regions of magnetic connectivity, that is, field lines connecting to different magnetic polarities at the photosphere. The boundaries or *separatrices* of these regions of connectivity are typical locations for magnetic reconnection, and so play an important role in AR dynamics (Longcope, 2005). In order to define separatrices that are discontinuous boundaries between different connectivity regions, null points (locations of zero magnetic field strength) are required. If, however, the AR magnetic field being studied does not contain null points, a generalization of separatrices known as *quasi-separatrix layers* (QSLs; Demoulin et al., 1996; Titov et al., 2002) may be employed. QSLs describe regions of strong, though not discontinuous, changes in connectivity mapping and so, like separatrices, are typical locations for magnetic reconnection.

As well as the identification of different topological regions within ARs, magnetic topology is also concerned with the structure of the magnetic field within these regions. One important element is how far from potential the magnetic field is, characterized through *twist* and *shearing*. Although quantities like twist and shearing may appear to be related to geometry rather than topology, they come under the umbrella of magnetic topology due to their connection with *magnetic helicity* (e.g., Berger & Field, 1984). Magnetic helicity is an invariant of both laminar and turbulent ideal magnetohydrodynamics (MHD) (Faraco & Lindberg, 2020; Faraco et al., 2022) and is approximately conserved even in the presence of weak resistivity (Berger, 1984). Magnetic helicity combines two fundamental quantities of magnetic fields: a measure of field line linkage and magnetic flux. It also has the property that it can be decomposed into *self* and *mutual* components, with the former related to the local twist of the magnetic field and the latter to sheared field (Berger & Field, 1984; Candelaresi et al., 2021). The magnitude of magnetic helicity is also well-known as a lower bound for magnetic energy (e.g., Berger, 1993). Further details of the topological interpretation of magnetic helicity, particularly in the context of magnetic fields in the solar atmosphere, can be found in Prior and MacTaggart (2020).

To summarize, in the context of ARs, magnetic topology is the description of the magnetic field's connectivity together with how it deviates from a potential field (via twist, shear, etc.). We now describe how we study magnetic topology in this work.

2.1. Magnetic Helicity and Winding Fluxes

One way to study magnetic topology directly from solar observations is to calculate *fluxes* of topological quantities through the photosphere. The topological quantities that we are discussing here are magnetic helicity, as mentioned above, and the related quantity of magnetic winding (MacTaggart et al., 2021; Prior & MacTaggart, 2020). Calculations of magnetic helicity flux are now standard for AR analysis. However, the interpretation of their signatures is not always straightforward. It has been suggested that one of the reasons for this is due to the fact that magnetic helicity is a combination of two fundamental properties - a measure of field line topology and magnetic flux. It has been shown that if magnetic helicity flux is renormalized, by removing its dependence on the magnetic field strength, then more information about magnetic topology related to near-horizontal magnetic field at the photosphere can be detected (MacTaggart & Prior, 2021; MacTaggart et al., 2021; Prior & MacTaggart, 2020). This renormalized quantity is called magnetic winding and, despite its close connection to magnetic helicity, it provides different information that is not available from magnetic helicity alone. Examples of its application include the identification of the emergence of pre-twisted magnetic fields (MacTaggart & Prior, 2021; MacTaggart et al., 2021) and the onset of CMEs signaled by changes in magnetic topology at the photosphere (Aslam et al., 2024). We now describe the calculation of magnetic helicity and winding fluxes.

Modeling the photosphere locally as a flat plane P (as for a magnetogram of an AR), the rates of change of magnetic helicity H and magnetic winding L through P are given by

$$\frac{\mathrm{d}H}{\mathrm{d}t} = \dot{H} = \int_P \frac{\mathrm{d}}{\mathrm{d}t}\mathcal{H}(\boldsymbol{x})\ \mathrm{d}^2x, \tag{1}$$

$$\frac{\mathrm{d}L}{\mathrm{d}t} = \dot{L} = \int_P \frac{\mathrm{d}}{\mathrm{d}t}\mathcal{L}(\boldsymbol{x})\ \mathrm{d}^2x, \tag{2}$$

where $\mathcal{H}$ is the field line helicity and $\mathcal{L}$ is the field line winding defined through

$$\frac{\mathrm{d}}{\mathrm{d}t}\mathcal{H}(\boldsymbol{x}) = \dot{\mathcal{H}} = -\frac{B_z(\boldsymbol{x})}{2\pi}\int_P \frac{\mathrm{d}}{\mathrm{d}t}\theta(\boldsymbol{x},\boldsymbol{y})B_z(\boldsymbol{y})\ \mathrm{d}^2y, \tag{3}$$

$$\frac{\mathrm{d}}{\mathrm{d}t}\mathcal{L}(\boldsymbol{x}) = \dot{\mathcal{L}} = -\frac{\sigma_z(\boldsymbol{x})}{2\pi}\int_P \frac{\mathrm{d}}{\mathrm{d}t}\theta(\boldsymbol{x},\boldsymbol{y})\sigma_z(\boldsymbol{y})\ \mathrm{d}^2y. \tag{4}$$

Here, σ_z is an indicator function for the sign of the component of the magnetic field orthogonal to P, that is,

$$\sigma_z = \begin{cases} 1 & \text{if} \quad B_z > 1, \\ -1 & \text{if} \quad B_z < 1, \\ 0 & \text{if} \quad B_z = 0, \end{cases} \tag{5}$$

and $\theta(\boldsymbol{x},\boldsymbol{y})$ is the pairwise winding angle of field line footpoints on P,

$$\theta(\boldsymbol{x},\boldsymbol{y}) = \arctan\left[\frac{(\boldsymbol{x}-\boldsymbol{y})\cdot\boldsymbol{e}_y}{(\boldsymbol{x}-\boldsymbol{y})\cdot\boldsymbol{e}_x}\right], \tag{6}$$

where we have made use of the standard Cartesian basis $\{\boldsymbol{e}_x,\boldsymbol{e}_y,\boldsymbol{e}_z\}$ with $\boldsymbol{e}_z$ directed upwards and orthogonal to P. Further details summarizing the theory and application of magnetic winding can be found in MacTaggart (2024).

In order to calculate the fluxes (H and L for time series, $\mathcal{H}$ and $\mathcal{L}$ for maps) we utilize the ARTop code (Alielden et al., 2023). This code makes use of Space-Weather Helioseismic and Magnetic Imager Active Region Patches

(SHARP) vector magnetograms and the DAVE4VM method for velocity fields. For the latter, an apodizing window of 20 pixels is used, as for the study by Aslam et al. (2024). Also, as in Aslam et al. (2024), any field strength less than 20 G in the magnetograms is ignored in the integrations. The SHARP patch containing AR13664 is 11149. In the north-eastern corner of this patch, traces of the weak active region AR13668 are present. However, this latter active region plays no role in the subsequent results and SHARP patch 11149 can be considered to represent AR13664.

2.2. NLFFF Extrapolations

In order to link topological winding signatures at the photosphere to the magnetic field in the atmosphere, we analyze NLFFF extrapolations. We use the method of Jarolim et al. (2023), which, for a magnetic field $\boldsymbol{B}$, satisfies the equations

$$(\nabla \times \boldsymbol{B}) \times \boldsymbol{B} = \boldsymbol{0}, \tag{7}$$

$$\nabla \cdot \boldsymbol{B} = 0. \tag{8}$$

Like ARTop, this NLFFF extrapolation procedure is also based on SHARP vector magnetograms. The purpose of using NLFFF extrapolations is to provide an efficient way of approximating the structure of the active region field that captures the main 3D topological features. For our purposes, we will analyze, in detail, magnetic features in an extrapolation at a particular time. To measure the accuracy of this extrapolation, we calculate the metrics of Wheatland et al. (2000). As a measure of how accurately the extrapolated solution represents a magnetic field, we determine the $\boldsymbol{B}$-weighted divergence averaged over the whole domain λ,

$$\lambda = \left\langle \frac{\|\nabla \cdot \boldsymbol{B}\|_2}{\|\boldsymbol{B}\|_2} \right\rangle. \tag{9}$$

Further, as a measure of force-freeness, we determine, at every grid point i, the sine of the angle between the current density and the magnetic field. Writing $F_i = \|(\nabla \times \boldsymbol{B}) \times \boldsymbol{B}\|_2$, $B_i = \|\boldsymbol{B}\|_2$ and $J_i = \|\nabla \times \boldsymbol{B}\|_2$ for the 2-norms evaluated at grid point i,

$$\sigma_i = \sin\theta_i = \frac{F_i}{B_i J_i}. \tag{10}$$

From this, a current-weighted measure of the angle is produced,

$$\theta_J = \arcsin\left(\frac{\sum_i J_i \sigma_i}{\sum_i J_i}\right). \tag{11}$$

Our analysis will focus on an extrapolation of AR13664 based on the SHARP patch at 04:36 UT on May 8th (details for this choice are presented later). The resulting extrapolation has metric values of $\lambda = 0.004$ and $\theta_J = 14.57°$. These values are in line with those reported by Jarolim et al. (2024) for the same active region. This level of accuracy is suitable for the analysis of this work and, as will be demonstrated later, the shapes of field lines produced by the extrapolation visibly match to features in related observations of the same region.

2.3. Flux Tube Topology

In line with our thesis that the emergence of a twisted magnetic flux tube leads to the eruption of the first halo CME, we now consider the topological signatures of twisted flux tube emergence. The understanding of how twisted magnetic field emerges from the convection zone into the solar atmosphere has been developed through many studies (mainly computational) over the past 25 years. Several reviews exist (Cheung & Isobe, 2014; Fan, 2021; Hood et al., 2012; Patsourakos et al., 2020) that summarize large aspects of this research effort. However, in order to provide more context for our results later, it is useful to describe some key elements of twisted flux tube emergence.

10.1029/2024JA033462

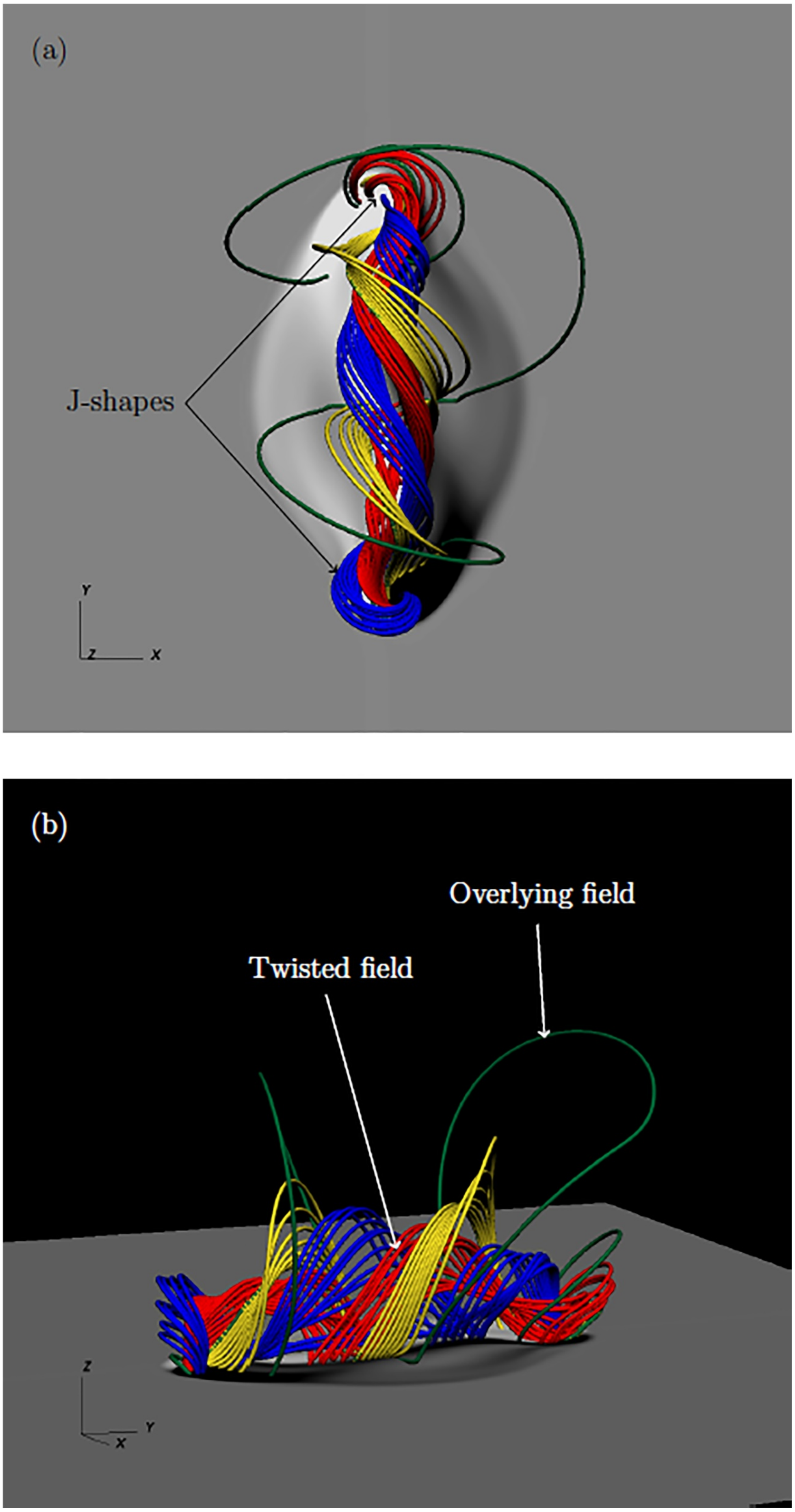

Figure 1. Two visualizations of the same snapshot from a simulation of a twisted magnetic flux tube emerging into the solar atmosphere. Different parts and topological features of the emerged field are identified with the use of different colored field lines.

Figure 1 displays two visualizations of a snapshot from a typical flux emergence simulation, simulating a twisted magnetic tube emerging into a hydrostatic atmosphere (e.g., Hood et al., 2012). The intention here is not to reproduce previous analysis but to use the figure to provide context useful for later discussions. Figure 1a displays an overhead view of emerged field lines above the photosphere, which is colored as a magnetogram of B_z ($B_z > 0$: white, $B_z < 0$: black). The red and blue field lines are traced from the main polarities of the region. Their twist creates the characteristic *J-shapes* (e.g., Archontis et al., 2009) that are indicated. The twisted field lines of the J-shapes travel along the direction of the polarity inversion line of the emerged region, creating *bald patches*, that is, locations where dips in the magnetic field at the photosphere are close to parallel with the photospheric plane P (Titov et al., 1993). This latter feature is most easily seen Figure 1b. Twisted magnetic field, as indicated by the yellow field lines, can penetrate high into the atmosphere and are contained in an overlying "magnetic envelope" field, as indicated by the green field lines. In the simulation shown in Figure 1, the only magnetic field present is that of the emerging flux tube. However, if the emerging field reconnects with pre-existing magnetic field in the solar atmosphere, this can also provide an overlying field for the emerging magnetic field (e.g., Archontis & Török, 2008; MacTaggart & Haynes, 2014).

All of these features are key indicators of twisted flux tube emergence and will play an important role in the analysis that follows. Although not shown here, eruptions from a magnetic field, such as that in Figure 1, can develop through the continued emergence and shearing of the magnetic field. This behavior can lead self-consistently, through magnetic reconnection, to the development of a new twisted flux tube in the atmosphere, which erupts as a CME (Archontis & Török, 2008; MacTaggart & Haynes, 2014; Patsourakos et al., 2020).

To summarize, if twisted flux tube emergence occurs, there are characteristic topological features (e.g., J-shapes, sheared field, bald patches) identified with the emergence of twisted magnetic field. Such signatures would be expected from NLFFF extrapolations.

3. Data Analysis

With the basic analysis approaches having been described, we now apply these to AR13664.

3.1. Flare Times and Winding Signatures

Figure 2 displays a time series of $\dot{L}$, calculated over the SHARP patch 11149, covering the period of the first halo CME on May 8th.

The time series of $\dot{L}$ provides a global (i.e., across the entire active region) measure of changes in pairwise winding angles of field lines at the photosphere (MacTaggart et al., 2021; Prior & MacTaggart, 2020). Large changes are indicative of significant topological changes. We consider a signature to be "large" if it substantially penetrates an envelope of $\mu \pm 2\sigma$, where μ is a running mean of $\dot{L}$ based on the previous hour's data and σ is a standard deviation. This identification has proved to be effective in other studies (e.g., Aslam et al., 2024). In addition to the winding time series, flare and CME times are superimposed on Figure 2. The flare times match the large winding spikes almost perfectly, differing by only a few minutes in each case. This observation indicates that there are significant topological changes at the photosphere co-temporal with these flares. However, more information is required in order to establish any causal link.

The flares (At the time of writing, these flares are cataloged on SolarMonitor (www.solarmonitor.org) as belonging to AR13665. However, the flare locator on SolarMonitor places both flares in AR13664, which is also indicated by a visual inspection of AIA data and our topological analysis.) occur before and after the detection of the first halo CME of AR13664 by the Large Angle and Spectrometric Coronagraph (LASCO) onboard the Solar and Heliospheric Observatory (SOHO) mission (Brueckner et al., 1995). The winding signature, approximately co-temporal with the X1.0 flare, occurs about 1 hour before the coronagraph detection of the CME. This time scale is typical of many CMEs and has been shown to be related to CME onset (Aslam et al., 2024). Furthermore, this time scale also approximately matches the time found by extrapolating a linear fit of LASCO observations of this CME back to the photosphere (The linear fit can be found at https://cdaw.gsfc.nasa.gov/CME_list/daily_plots/sephtx/2024_05/sephtx_20240508.png, with the approximated time of the CME near the solar surface being in close proximity to the start time of the X1.0 flare.). These observations further suggest that not only may the first winding signature and X1.0 flare be related but that they may also be linked to the onset of the halo CME. The

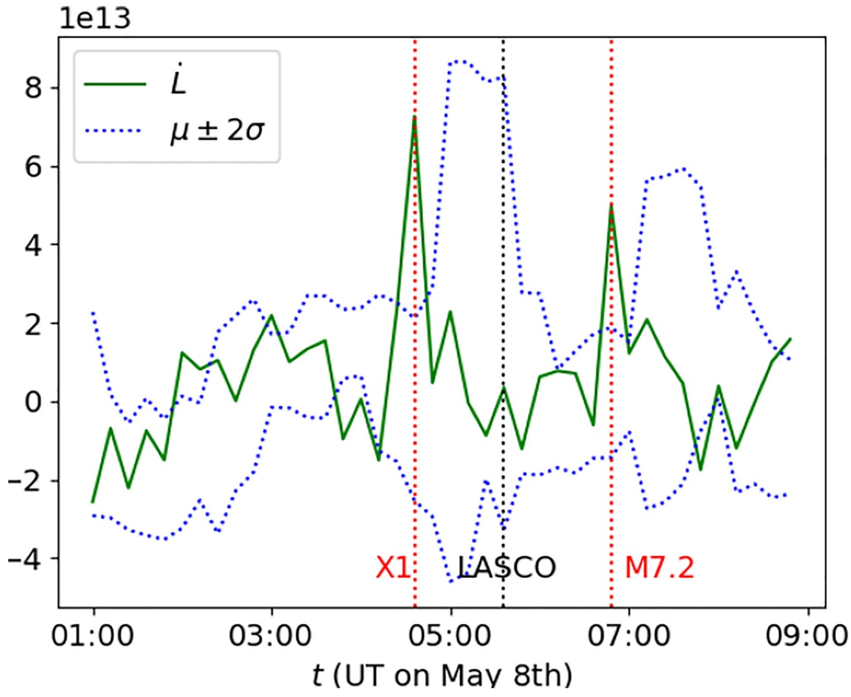

Figure 2. Time series of $\dot{L}$ (units: km^4 s^{-1}; green line) with an envelope of two standard deviations (blue dotted lines) either side of a running mean based on the previous hour's data. The running mean is not shown. The start times of X1.0 and M7.2 flares are indicated (dotted red lines), as is the time of the first halo CME of AR13664 recorded by LASCO (black dotted line).

establishment of this connection means that the source of the enhanced eruptive activity of AR13664 can be identified. We now investigate this possibility through a detailed analysis of the magnetic topology of AR13664.

3.2. Topological Sub-Regions

In order to understand and identify the key magnetic structure responsible for the first halo CME of AR13664, we need to understand the global magnetic topology of the AR. To do this, we make use of a NLFFF extrapolation. Figure 3 displays two maps of AR13664 just before the start time of the X1.0 flare: a magnetogram of the out-of-plane magnetic field component B_z and an Atmospheric Imaging Assembly (AIA) 193 Åmap, indicative of coronal temperatures (Lemen et al., 2012).

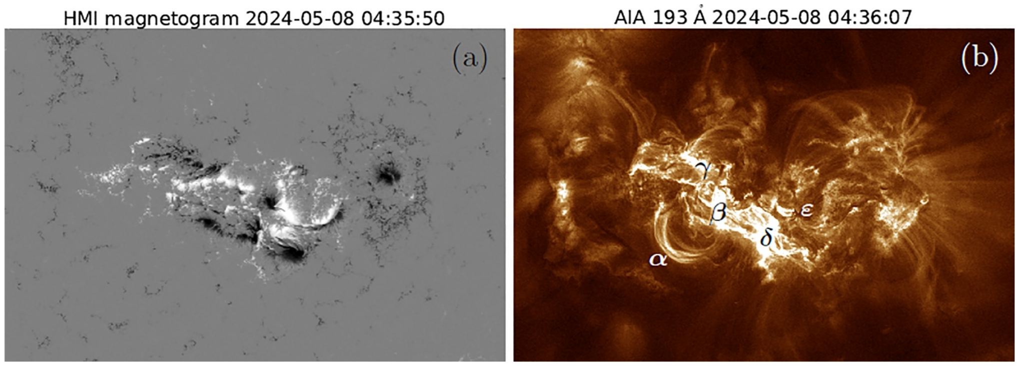

Figure 3. The SHARP region 11149 (dominated by AR13664) just before the start time of the X1.0 flare. Panel (a) displays a magnetogram of B_z (the magnetic component orthogonal to the magnetogram plane) and panel (b) shows an AIA 193 Å intensity map. Four regions of high intensity in (b) are labeled α, β, γ and δ. The remaining region, labeled ε, is included for reference to discussions later.

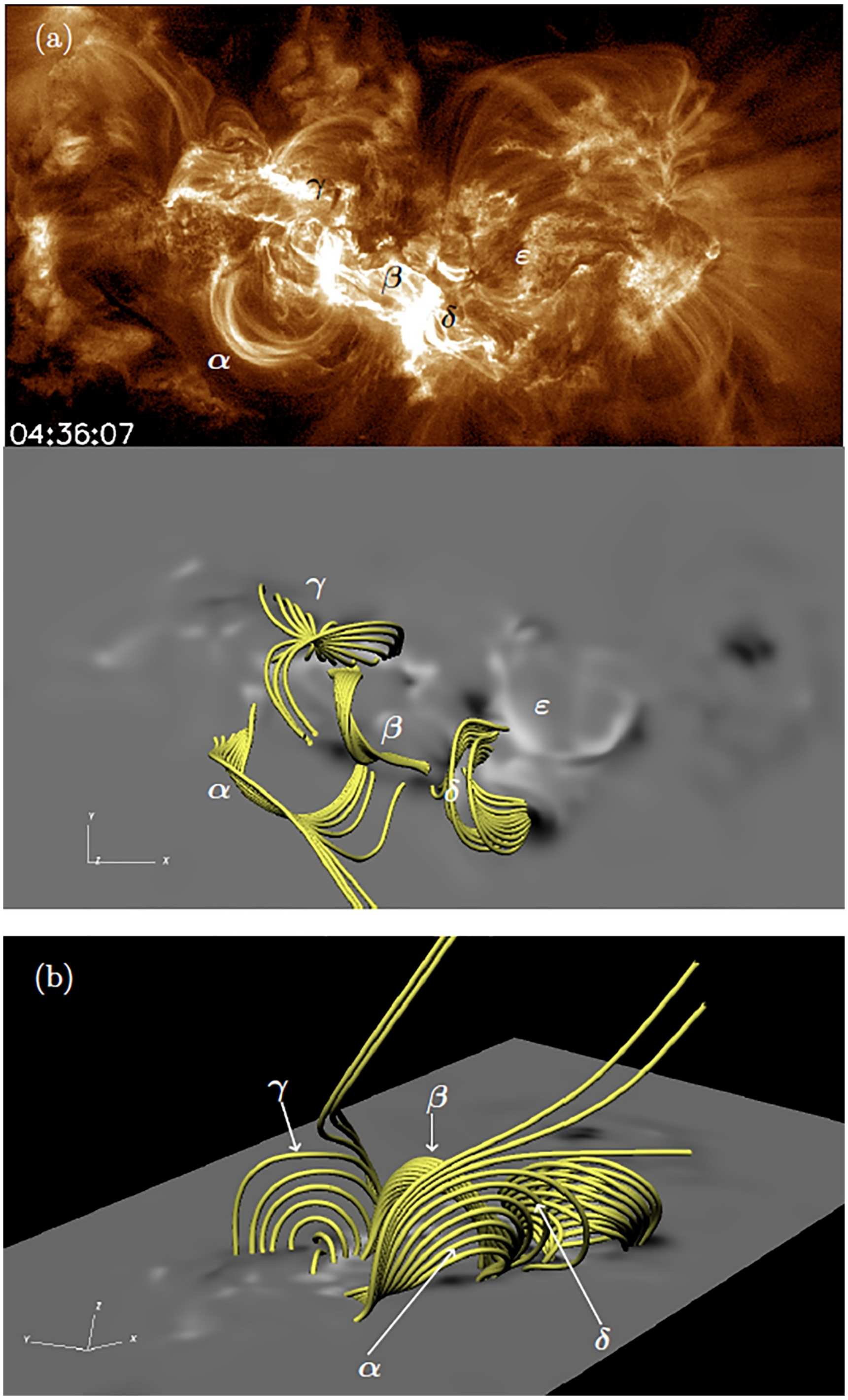

Figure 4. NLFFF extrapolation of the magnetic field of AR13664 on May 8th at 04:36UT. Field lines are traced based on the features α, β, γ and δ from Figure 3b, which is reproduced here for reference. The label ε is included for use in discussions later in the main text. Panel (b) shows the same field lines from a different viewpoint.

The regions of stronger intensity in the AIA map provide structures with which a NLFFF extrapolation may be compared. That is, if a NLFFF extrapolation is to represent a good approximation of the magnetic field of AR13664, its field line geometry should show some correspondence to the structures identified in the AIA map. To this end, four sub-regions of enhanced intensity are identified on the AIA map and labeled α, β, γ and δ. An additional label ε, not related to any particular region of intense emission, is included for use in discussions later.

At each of the first four locations, field lines in a NLFFF extrapolation have been plotted to relate particular magnetic structures to these regions of higher intensity. The field lines are displayed in Figure 4, and the extrapolation corresponds to the time of the recorded winding spike at 04:36 UT on May 8th.

A comparison of the sub-regions identified in Figure 3 with the field lines in Figure 4a reveals that the NLFFF extrapolation is able to trace out the main features seen in the AIA map. For the feature at α, the intensity loops correspond to curved field lines of a similar shape. For the feature at β, the north-south-oriented patch of intensity at one set of footpoints of the α feature matches well with a twisted magnetic field lines connecting a bipolar region at the center of AR13664. For the feature at γ, the region of higher intensity corresponds to a sheared arcade near the top of AR13664 (see Figure 4b for a clear representation of the magnetic shear). Finally, the feature at δ also matches well with the corresponding field line geometry with field lines that form a boundary beside sub-region β. To summarize, the NLFFF extrapolation is able to reproduce the shapes of the identified sub-regions of higher intensity in the AIA 193 Åmap, all of which correspond to sub-regions of twisted magnetic field, and are thus all potential candidates for being the source of free magnetic energy required to create the first halo CME.

The aforementioned positive winding spike at the time of the X1.0 flare in Figure 2 is based on integrating over the entire SHARP patch. In order to relate this spike to particular sub-regions, we produce contour maps of $\dot{\mathcal{L}}$ and examine the large-scale winding signatures within these features. Figure 5 presents contours of $\dot{\mathcal{L}}$ overlaid on magnetograms, zooming in on different parts of the active region and identifying the dominant winding signatures with red boxes, for ease of visualization. Like the NLFFF extrapolation, these maps are based on SHARP magnetograms on May 8th at 04:36UT.

Figures 5a and 5b highlight the dominant (in terms of magnitude and physical extension) winding signatures. The locations of these dominant signatures correspond to the sub-regions indicated by β and ε respectively in Figures 3b and 4a. Each of these sub-regions is now discussed in detail.

3.3. Western (β) Sub-Region

As reported by Romano et al. (2024), bipolar regions emerged on the western side of AR13664 during the May 5th and 6th. The first such emergence led to the magnetic bipolar region that can be seen at the north-west of AR13664, with the negative polarity stretching from 338° to 343° Carrington longitude between latitudes of −16° and −17° in Figure 5a. This region later collided with a larger bipolar region in the center of AR13664 which, by the time of the X1.0 flare, occupies the Carrington longitudes 338° to 346° and latitudes −17° to −22°, as shown in Figure 5a, and corresponds to sub-region β. As well as the evidence from Romano et al. (2024) and Kontogiannis (2024) that this region was formed by emergence, we can also make use of magnetic helicity and winding fluxes to show that magnetic field with bulk twist emerged in this sub-region. First, we select a time, May 6th at 21:00 UT, during the emergence that is typical of the behavior of this sub-region during this period. In Figure 6, a line-of-sight magnetogram is displayed together with the line-of-sight component of the field line velocity, that is, the velocity estimate derived from inverting the ideal induction equation via the DAVE4VM method. In Figure 6a the two polarities of the emerging region can be seen. As shown by Romano et al. (2024) these polarities move in a north-south direction. The lower negative polarity is shown colliding with a pre-existing positive polarity. In Figure 6b, the line-of-sight velocity is positive for large patches within the emerging region. This upward motion is particularly strong at Carrington longitude 344°. The strongest upflow can be seen at the boundary of the emerging region, buffered by a region of strong negative velocity just outside the emerging region. Figure 7 displays the corresponding maps of $\dot{\mathcal{H}}$ and $\dot{\mathcal{L}}$ at this time and, for comparison, the later time of May 7th at 00:00 UT. In Figures 7a and 7b, the background map shows the field line helicity rate $\dot{\mathcal{H}}$ and the contours show the field line winding rate $\dot{\mathcal{L}}$. The helicity maps follow closely the magnetograms of B_z, given the strong dependence of $\dot{\mathcal{H}}$ on B_z (see Equation 3). In Figure 7a, the key feature is that the field line winding rate has a strong concentration between the main polarities, with peaks overlapping with the stronger patches of the line-of-sight component of the field line velocity, shown in Figure 6b. The signature of $\dot{\mathcal{L}}$ is dominated by changes in the footpoint winding angles of field lines due, primarily, to the upward motion of those field lines as they emerge through the photosphere. The same qualitative behavior can also be seen in at the later time shown in Figure 7b. The irregular shapes of the winding signatures are due to the interaction of the magnetic field with convection, which emerges

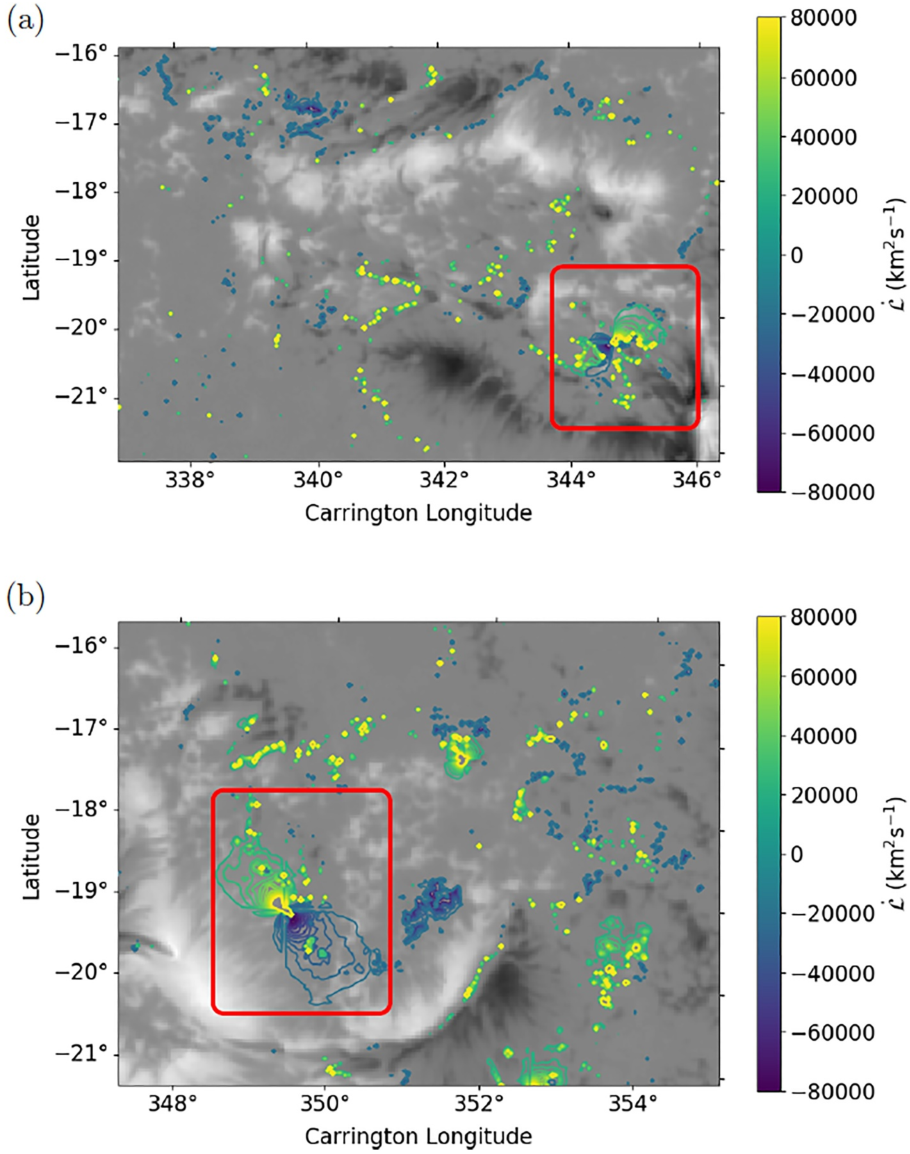

Figure 5. Contours of $\dot{\mathcal{L}}$ superimposed on magnetograms of B_z of AR13664 on May 8th at 04:36UT. Panel (a) focuses on the western part of the active region and panel (b) on the eastern part. The dominant winding signatures are highlighted with red boxes.

in stages (MacTaggart et al., 2021). Once most of the field has emerged, if it corresponds to a twisted flux tube, the emerged field in the atmosphere should have a bulk twist. We will come back to this point shortly.

Returning to the winding map of Figure 5a, at a time after the main emergence phase, there is a strong winding signature in the south-eastern corner of sub-region β, highlighted with a red box. This signature corresponds to a rapid change in the winding angles between field line footpoints in this location. Possible causes could be the emergence or submergence of locally twisted field lines. In order to understand how this signature relates to the magnetic topology in the atmosphere, we use its location as a starting point for tracing field lines. That is, we take the location of the peak of the winding signature on the magnetogram and follow field lines traced from seed points on a line fixed to that point and orthogonal to the magnetogram plane.

In Figure 8, field lines are color-coded depending on their seed locations. The red field lines are traced from the dominant winding signature of Figure 5a. These field lines result in two structures: a J-shape and twisted field lines connected to the other side of the bipole. The J-shape forms a bald patch at the location of the dominant

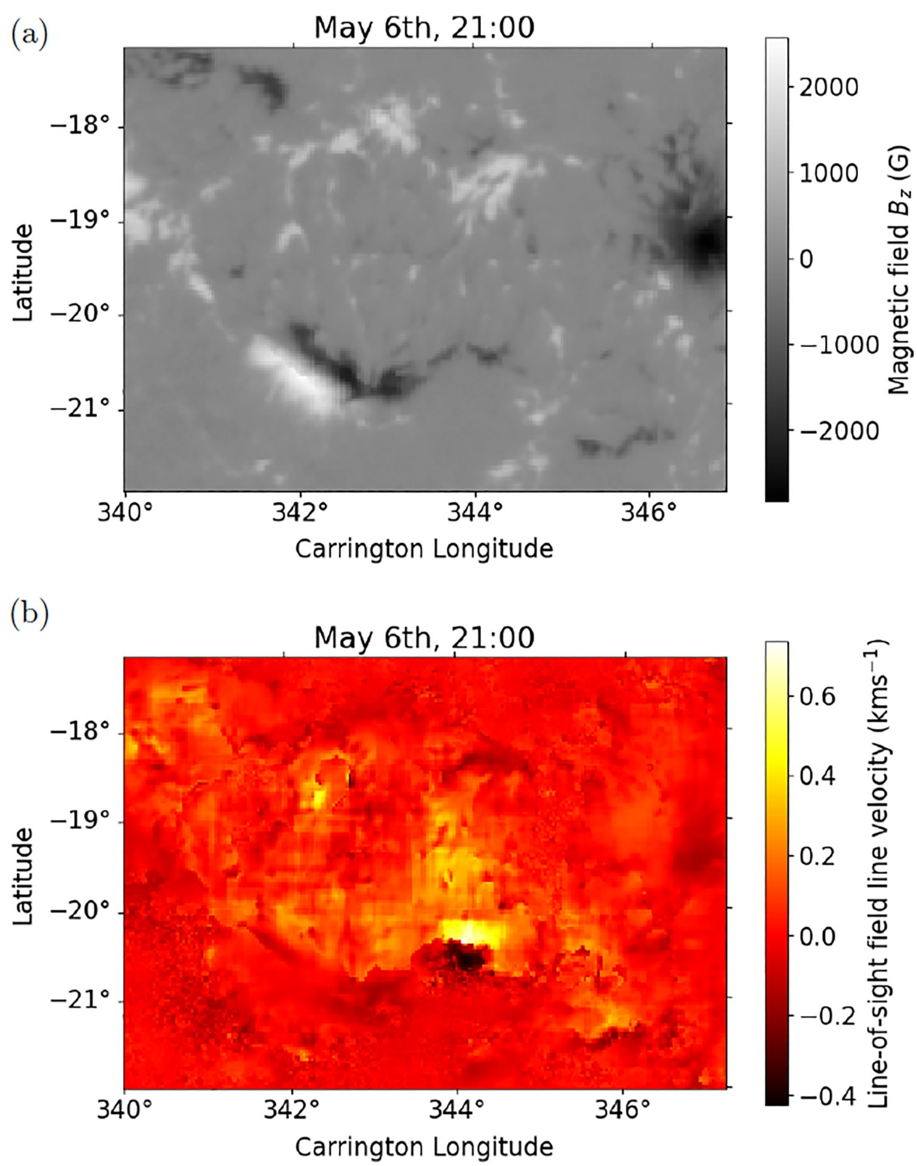

Figure 6. Maps of sub-region β on May 6th at 21:00 UT, showing (a) B_z and (b) the line-of-sight field line velocity.

winding signature and this signature has also been found in relation to other CME onsets (Aslam et al., 2024). In terms of flux tube topology described earlier (see Figure 1), the red field lines form an important part of this overall picture. At the other end of the bipolar region, blue field lines mirror the behavior of the red field lines. Almost orthogonal to the twisted field, higher overlying field (shown as green field lines) provides an overlying magnetic arcade for the twisted field lower in the atmosphere. The field lines associated with the β sub-region in Figure 4a are also overlying field lines, though traced at different locations. Finally, to emphasize the twist of the magnetic field within the β sub-region, yellow field lines wrap around the blue and red field lines whilst remaining lower than the overlying field.

To summarize, in addition to the descriptions in Romano et al. (2024) and Kontogiannis (2024), our topological analysis is in line with the interpretation that sub-region β is the result of an emerging twisted flux tube. Magnetic helicity and winding fluxes indicate that twisted magnetic field emerges into the atmosphere. After this period of emergence, and by the time of the X1.0 flare, the NLFFF extrapolation captures the large-scale features of the magnetic field in this sub-region and reveals a magnetic field with a bulk twist and the classical characteristics of an emerged twisted flux tube. The emergence of a twisted flux tube into an overlying magnetic field that is already far from potential makes the magnetic field in sub-region β a prime candidate for the source of the first halo CME.

10.1029/2024JA033462

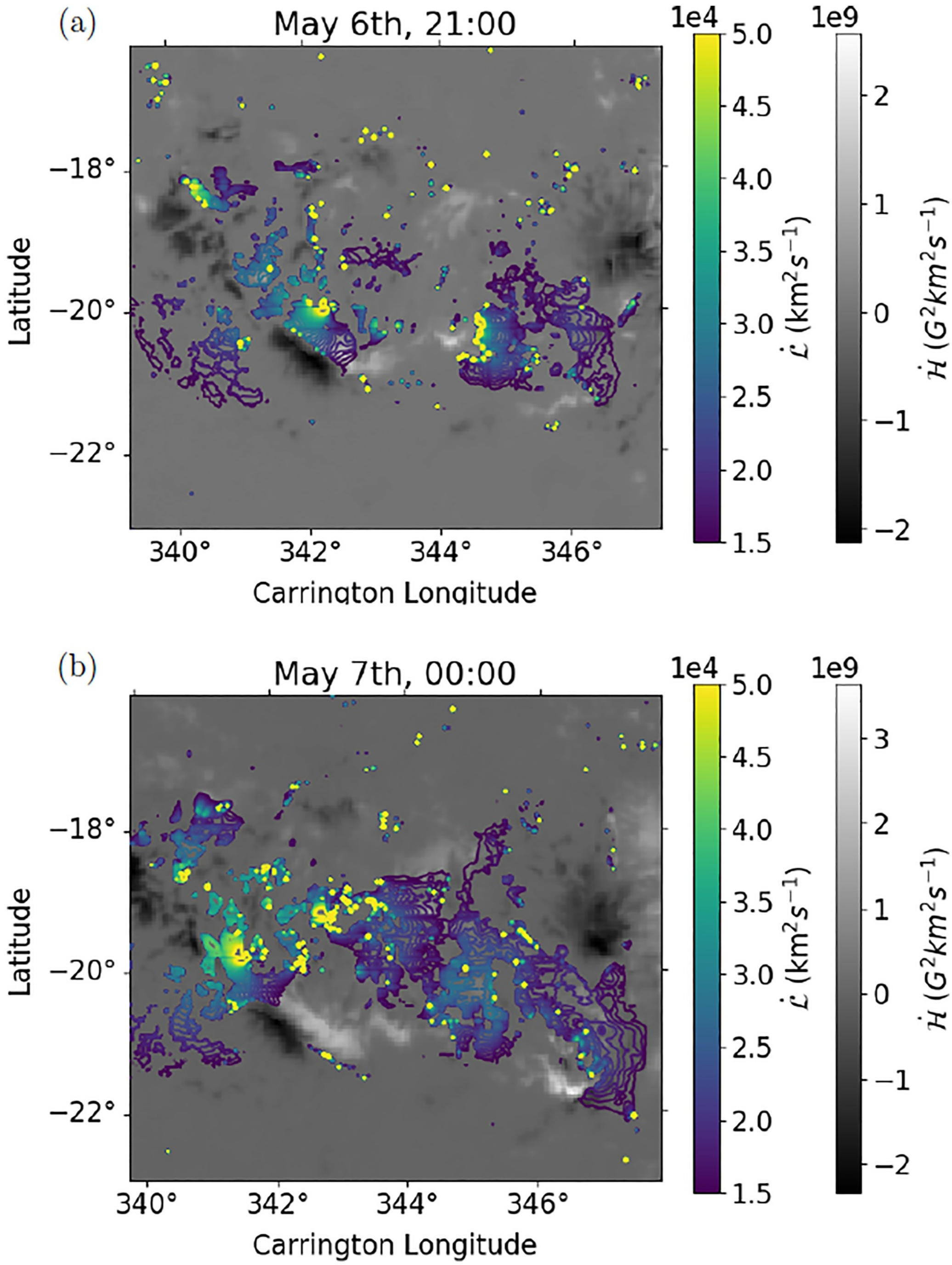

Figure 7. Maps of $\dot{\mathcal{H}}$ with contours of $\dot{\mathcal{L}}$ within sub-region β on (a) May 6th at 21:00 UT and (b) May 7th at 00:00 UT.

3.4. Eastern (ε) Sub-Region

We now consider the second dominant winding signature, shown in Figure 5b. Field lines related to this signature are displayed in Figure 9.

The field lines traced in red have their seeds at the location of the dominant winding signature in Figure 5b. These field lines form a dome-like structure covering the pre-existing part of AR13664 (as opposed to the later emerging bipole regions). The dominant winding signature corresponds to a section of near-horizontal magnetic field, that is, a bald patch. This older part of the active region continues to evolve in time (see Romano et al. (2024) for the

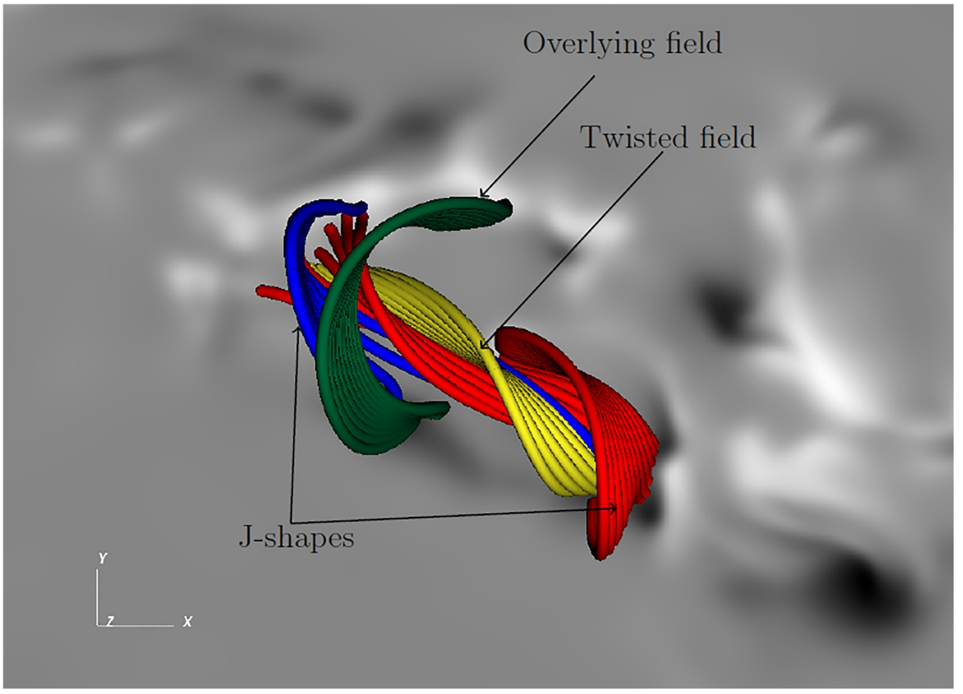

Figure 8. Field lines of the NLFFF extrapolation of AR13664 on May 8th at 04:36 UT traced within the central emerging bipole. The red field lines are traced from the location of the dominant winding signature in Figure 5a. The blue field lines are traced from the photosphere at the opposite end of the bipole. The green field lines are traced higher in the atmosphere and the yellow field lines are traced from between the red and blue central field lines and the green field lines. Labels relating the resulting structures to flux tube topology are indicated.

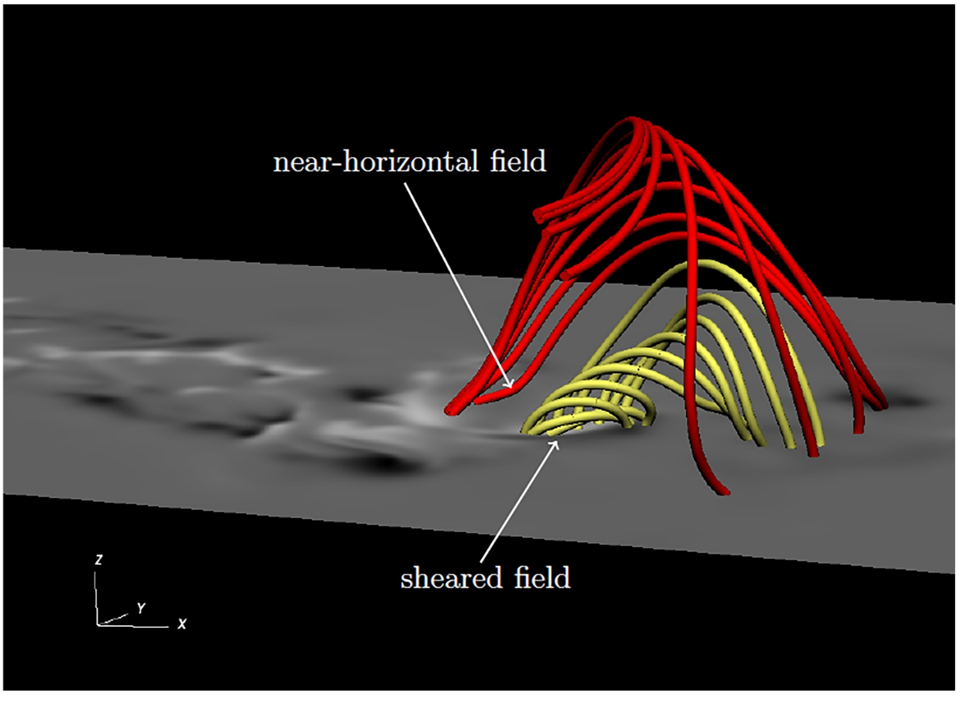

Figure 9. Field lines of the NLFFF extrapolation of AR13664 on May 8th at 04:36 UT traced on the eastern side of the active region. The red field lines are traced from the location of the dominant winding signature in Figure 5b. This signature corresponds to the near-horizontal field indicated. Nearby field lines are traced in yellow, highlighting a region of highly sheared field.

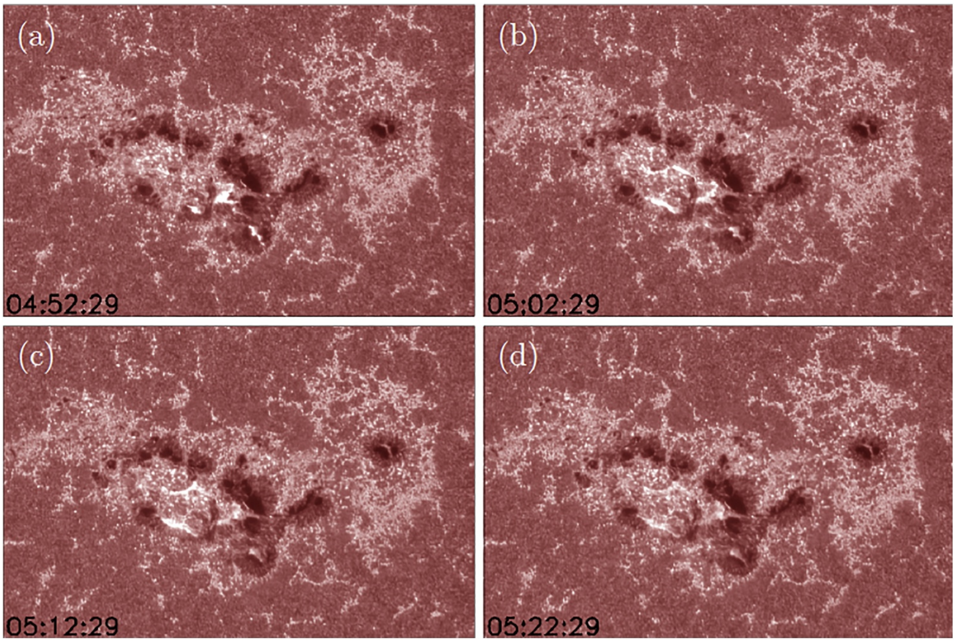

Figure 10. Maps of AIA 1700 Å for AR13664 at four different times corresponding to the growth and decay of flare ribbons related to the first halo CME. The parallel ribbons can be seen most clearly in (b).

evolution of photospheric magnetic and velocity fields). Part of this evolution has led to the creation of a curved polarity inversion line (see Figure 5b at (352°,-20°)) with highly sheared magnetic field. Similar to sub-region β, there is a magnetic configuration in sub-region ε that has the potential to produce a flare or CME.

3.5. Magnetic Origin of the X1.0 Flare and Halo CME

Based on the dominant winding signatures in sub-regions β and ε, we have identified two magnetic configurations that have the potential to be the source of the X1.0 flare and/or the first halo CME. To determine which of these is responsible, we examine the behavior of the *flare ribbons* associated with the X1.0 flare of the CME. Flare ribbons are regions of increased emission in the lower atmosphere that are signatures of energy deposited from CME (and associated flare) eruptions (see Benz, 2008, and references within). Flare ribbons trace out the footpoints of the magnetic field in the lower atmosphere and their pattern depends on the magnetic topology. For example, in the context of the "standard" flare model (see, for example, Figure 1 of Asai et al., 2004), two (approximately) parallel ribbons would be expected as a magnetic arcade is present beneath the erupting CME flux rope. Subsequently, the ribbons would trace the footpoints of the arcade (Fletcher & Hudson, 2001; Masuda et al., 2001). For a magnetic field with the flux tube topology described earlier, a CME in this context follows the standard model, and so two parallel ribbons would be expected. Figure 10 displays maps of AIA 1700 Åfor AR13664 after the start time of the X1.0 flare and before the LASCO observation of the CME. Ultraviolet emission at this wavelength is often taken as evidence of plasma heating in the lower solar atmosphere, showing where energy from an eruption is deposited (Fletcher & Hudson, 2001). These maps can thus be used to visualize flare ribbons.

The structure of AR13664 can easily be recognized in the AIA 1700 Åmaps, with the large emerged bipole occupying the center-left of the images. The first brightening shown in Figure 10a lies near to the position of the dominant winding signature in Figure 5a. Based on the NLFFF extrapolation, this corresponds to the eastern (of the emerged bipole) J-shape which is nearly horizontal to the photosphere at this location. In Figures 10b and 10c, two parallel ribbons are clearly seen, which follow the lines of the footpoints of the overlying magnetic arcade (shown in green in Figure 4), whilst Figure 10d shows that the brightenings begin to weaken (a video showing the time evolution of the brightenings can be found at https://sdo.gsfc.nasa.gov/data/dailymov/movie.php?q=20240508_1024_1700). By this stage, the CME is already in ascent and, approximately 13 min later, will be detected by the LASCO coronagraph. The observed pattern of brightenings follow that of the standard model described above. For a clearer comparison of the ribbons with the magnetic field, the map containing the strongest

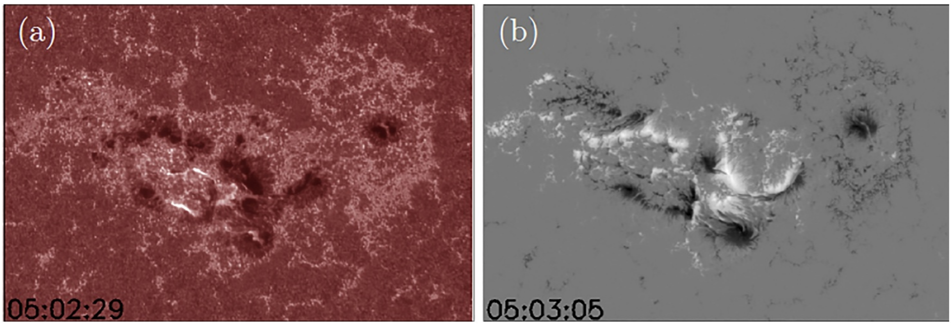

Figure 11. A visualization of the AIA 1700 Å map displayed in Figure 10, showing parallel flare ribbons, beside its corresponding line-of-sight magnetogram.

brightenings at 1700 Å (Figure 10b) is reproduced in Figure 11a beside its corresponding magnetogram in Figure 11b.

As there are no brightenings at the ε sub-region, we attribute the origin of the X1.0 flare and the halo CME to be the central emerging sub-region in AR13664, which our evidence points to being an emerging, and subsequently erupting, twisted flux tube.

3.6. M7.2 Flare

The magnetic configuration identified in sub-region ε also led to eruptive behavior, although later than the first halo CME. In Figure 2, a winding spike was shown to be co-temporal with the start time of a M7.2 flare. Rather than repeat the entire analysis for this time, we take note of associated flare ribbons in relation to the magnetic topology that we have already examined. In Figure 12, the AIA 1700 Åmaps for AR13664 (immediately before and after the M7.2 flare, which had a start time at 06:44UT) reveal that the overall structure of the active region largely unchanged from this flare. The position of the flare ribbon in Figure 12b corresponds to the sheared field identified in Figure 9.

4. Summary

In this work, we have investigated observations of AR13664 to identify the magnetic source of its first halo CME, and thus of its period of enhanced eruptive activity. Basing our analysis on SHARP vector magnetograms and maps of AIA intensity, we have studied the magnetic topology of AR13664 through the calculation of fluxes of magnetic helicity and winding, together with NLFFF extrapolations. By combining these methods of analysis, we identified a sub-region of AR13664 that is coherent with being generated by the emergence of a twisted flux tube. In terms of our topological analysis, this is first evidenced by maps of $\dot{\mathcal{L}}$ and $\dot{\mathcal{H}}$, indicating the emergence of pre-twisted magnetic field between the two magnetic footpoints of the emerging sub-region. After the emergence phase, at the onset time of the CME, a NLFFF extrapolation reveals a magnetic field in the sub-region with a bulk twist and field line topology in line with what is expected from the emergence of a twisted flux tube. The first halo

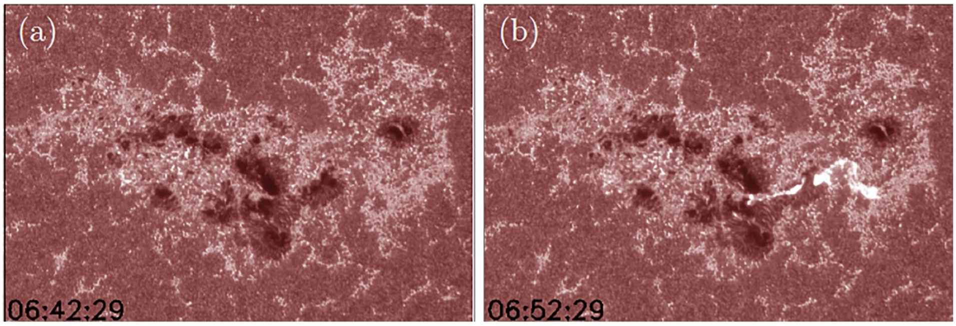

Figure 12. Maps of AIA 1700 Å for AR13664 at two different times before and after the M7.2 flare.

CME had an associated X1.0 flare. Post-flare (and post-CME) ribbons were found to follow near-parallel paths near the edges of the emerged flux tube. All of these elements point toward the emergence of a twisted flux tube within AR13664 being the driver of its first halo CME.

The analysis developed in this work can also be applied to other eruptions in this AR, or any eruptive AR. In identifying the source of the first halo CME, our analysis revealed two possible sub-regions as candidates. As a postscript to the main analysis, we showed that the sub-region that was not responsible for the CME, shortly afterward was the location of a M7.2 flare.

Data Availability Statement

The ARTop code, used for calculating winding signatures, can be found at https://github.com/DavidMacT/ARTop. The code for producing NLFFF extrapolations can be found at https://github.com/RobertJaro/NF2.

Acknowledgments
The authors would like to thank Roberto Battiston for helpful discussions. DM and OPMA acknowledge support from a Leverhulme Trust Grant (RPG-2023-182). DM also acknowledges support from a Science and Technologies Facilities Council (STFC) Grant (ST/Y001672/1) and a Personal Fellowship from the Royal Society of Edinburgh (ID: 4282). TW acknowledges support from the US Air Force grant FA8655-23-1-7247. Version 6.0.1 of the SunPy open source software package (The SunPy Community et al., 2020) was used for this research.

References

Alielden, K., MacTaggart, D., Ming, Q., Prior, C., & Raphaldini, B. (2023). ARTop: An open-source tool for measuring active region topology at the solar photosphere. *RAS Techniques and Instruments*, *2*(1), 398–407. https://doi.org/10.1093/rasti/rzad029

Archontis, V., Hood, A. W., Savcheva, A., Golub, L., & Deluca, E. (2009). On the structure and evolution of complexity in sigmoids: A flux emergence model. *The Astrophysical Journal*, *691*(2), 1276–1291. https://doi.org/10.1088/0004-637x/691/2/1276

Archontis, V., & Török, T. (2008). Eruption of magnetic flux ropes during flux emergence. *Astronomy & Astrophysics*, *492*(2), L35–L38.

Asai, A., Yokoyama, T., Shimojo, M., Masuda, S., Kurokawa, H., & Shibata, K. (2004). Flare ribbon expansion and energy release rate. *The Astrophysical Journal*, *611*(1), 557–567. https://doi.org/10.1086/422159

Aslam, O. P. M., MacTaggart, D., Williams, T., Fletcher, L., & Romano, P. (2024). Photospheric signatures of CME onset. *Monthly Notices of the Royal Astronomical Society*, *534*(1), 444–454. https://doi.org/10.1093/mnras/stae2110

Bai, T. (1988). Distribution of flares on the Sun during 1955–1985: "hot spots" (active zones) lasting for 30 years. *The Astrophysical Journal*, *328*, 860. https://doi.org/10.1086/166344

Barnes, W. T., Barnes, W. T., Bobra, M. G., Christe, S. D., Freij, N., Hayes, L. A., et al. (2020). The SunPy project: Open source development and status of the version 1.0 core package. *The Astrophysical Journal*, *890*(1), 68. https://doi.org/10.3847/1538-4357/ab4f7a

Benz, A. O. (2008). Flare observations. *Living Reviews in Solar Physics*, *5*(1), 1. https://doi.org/10.12942/lrsp-2008-1

Berger, M. A. (1984). Rigorous new limits on magnetic helicity dissipation in the solar corona. *Geophysical & Astrophysical Fluid Dynamics*, *30*(1–2), 79–104. https://doi.org/10.1080/03091928408210078

Berger, M. A. (1993). Energy-crossing number relations for braided magnetic fields. *Physical Review Letters*, *70*(6), 705–708. https://doi.org/10.1103/PhysRevLett.70.705

Berger, M. A., & Field, G. B. (1984). The topological properties of magnetic helicity. *Journal of Fluid Mechanics*, *147*(-1), 133–148. https://doi.org/10.1017/s0022112084002019

Brueckner, G. E., Howard, R. A., Koomen, M. J., Korendyke, C. M., Michels, D. J., Moses, J. D., et al. (1995). The Large Angle Spectroscopic Coronagraph (LASCO). *Solar Physics*, *162*(1–2), 357–402. https://doi.org/10.1007/978-94-009-0191-9_10

Candelaresi, S., Hornig, G., MacTaggart, D., & Simitev, R. D. (2021). On self and mutual winding helicity. *Communications in Nonlinear Science and Numerical Simulation*, *103*, 106015. https://doi.org/10.1016/j.cnsns.2021.106015

Cheung, M. C. M., & Isobe, H. (2014). Flux emergence (theory). *Living Reviews in Solar Physics*, *11*(1), 3. https://doi.org/10.12942/lrsp-2014-3

Demoulin, P., Henoux, J. C., Priest, E. R., & Mandrini, C. H. (1996). Quasi-separatrix layers in solar flares. I. Method. *Astronomy & Astrophysics*, *308*, 643–655.

Fan, Y. (2021). Magnetic fields in the solar convection zone. *Living Reviews in Solar Physics*, *18*(1), 5. https://doi.org/10.1007/s41116-021-00031-2

Faraco, D., & Lindberg, S. (2020). Proof of Taylor's conjecture on magnetic helicity conservation. *Communications in Mathematical Physics*, *373*(2), 707–738. https://doi.org/10.1007/s00220-019-03422-7

Faraco, D., Lindberg, S., MacTaggart, D., & Valli, A. (2022). On the proof of Taylor's conjecture in multiply connected domains. *Applied Mathematics Letters*, *124*, 107654. Paper No. 107654, 7. https://doi.org/10.1016/j.aml.2021.107654

Fletcher, L., & Hudson, H. (2001). The magnetic structure and generation of EUV flare ribbons. *Solar Physics*, *204*(1/2), 69–89. https://doi.org/10.1023/A:1014275821318

Hoeksema, J. T., Liu, Y., Hayashi, K., Sun, X., Schou, J., Couvidat, S., et al. (2014). The Helioseismic and Magnetic Imager (HMI) vector magnetic field pipeline: Overview and performance. *Solar Physics*, *289*(9), 3483–3530. https://doi.org/10.1007/s11207-014-0516-8

Hood, A. W., Archontis, V., & MacTaggart, D. (2012). 3D MHD flux emergence experiments: Idealised models and coronal interactions. *Solar Physics*, *278*(1), 3–31. https://doi.org/10.1007/s11207-011-9745-2

Jarolim, R., Thalmann, J. K., Veronig, A. M., & Podladchikova, T. (2023). Probing the solar coronal magnetic field with physics-informed neural networks. *Nature Astronomy*, *7*(10), 1171–1179. https://doi.org/10.1038/s41550-023-02030-9

Jarolim, R., Veronig, A., Purkhart, S., Zhang, P., & Rempel, M. (2024). Magnetic field evolution of the solar active region 13664. *The Astrophysical Journal*, *976*(1). https://iopscience.iop.org/article/10.3847/2041-8213/ad8914

Jaswal, P., Sinha, S., & Nandy, D. (2025). Deconstructing solar super active region 13664 in the context of the historic geomagnetic storm of 2024 May 10-11. *The Astrophysical Journal*, *979*(1). https://iopscience.iop.org/article/10.3847/1538-4357/ad960b

Kontogiannis, I. (2024). The extremely strong non-neutralized electric currents of the unique solar active region NOAA 13664. *Astronomy & Astrophysics*, *690*(L10), 5. https://www.aanda.org/articles/aa/full_html/2024/10/aa51627-24/aa51627-24.html

Lemen, J. R., Title, A. M., Akin, D. J., Boerner, P. F., Chou, C., Drake, J. F., et al. (2012). The Atmospheric Imaging Assembly (AIA) on the Solar Dynamics Observatory (SDO). *Solar Physics*, *275*(1–2), 17–40. https://doi.org/10.1007/978-1-4614-3673-7_3

Longcope, D. W. (2005). Topological methods for the analysis of solar magnetic fields. *Living Reviews in Solar Physics*, *2*(1), 7. https://doi.org/10.12942/lrsp-2005-7

MacTaggart, D. (2024). Magnetic winding: Theory and applications. In K. Kuzanyan, N. Yokoi, M. K. Georgoulis, & R. Stepanov (Eds.), *Helicities in geophysics, astrophysics, and beyond* (Vol. 283, pp. 17–24). https://doi.org/10.1002/9781119841715.ch2

MacTaggart, D., & Haynes, A. L. (2014). On magnetic reconnection and flux rope topology in solar flux emergence. *Monthly Notices of the Royal Astronomical Society*, *438*(2), 1500–1506. https://doi.org/10.1093/mnras/stt2285

MacTaggart, D., & Prior, C. (2021). Helicity and winding fluxes as indicators of twisted flux emergence. *Geophysical & Astrophysical Fluid Dynamics*, *115*(1), 85–124. https://doi.org/10.1080/03091929.2020.1740925

MacTaggart, D., Prior, C., Raphaldini, B., Romano, P., & Guglielmino, S. L. (2021). Direct evidence that twisted flux tube emergence creates solar active regions. *Nature Communications*, *12*(1), 6621. https://doi.org/10.1038/s41467-021-26981-7

Masuda, S., Kosugi, T., & Hudson, H. S. (2001). A hard X-ray two-ribbon flare observed with Yohkoh/HXT. *Solar Physics*, *204*, 55–67.

Patsourakos, S., Vourlidas, A., Török, T., Kliem, B., Antiochos, S. K., Archontis, V., et al. (2020). Decoding the pre-eruptive magnetic field configurations of coronal mass ejections. *Space Science Reviews*, *216*(8), 131. https://doi.org/10.1007/s11214-020-00757-9

Pesnell, W. D., Thompson, B. J., & Chamberlin, P. C. (2012). The Solar Dynamics Observatory (SDO). *Solar Physics*, *275*(1–2), 3–15. https://doi.org/10.1007/s11207-011-9841-3

Priest, E., & Forbes, T. (2000). *Magnetic reconnection: MHD theory and applications*. Cambridge University Press.

Prior, C., & MacTaggart, D. (2020). Magnetic winding: What is it and what is it good for? *Proceedings of the Royal Society of London Series A*, *476*(2242), 20200483. https://doi.org/10.1098/rspa.2020.0483

Romano, P., Elmhamdi, A., Marassi, A., & Contarino, L. (2024). Analyzing the sequence of phases leading to the formation of the active region 13664, with potential Carrington-like characteristics. *The Astrophysical Journal Letters*, *973*(1), L31. https://doi.org/10.3847/2041-8213/ad77cb

Schuck, P. W. (2008). Tracking vector magnetograms with the magnetic induction equation. *The Astrophysical Journal*, *683*(2), 1134–1152. https://doi.org/10.1086/589434

Titov, V. S., Hornig, G., & Démoulin, P. (2002). Theory of magnetic connectivity in the solar corona. *Journal of Geophysical Research (Space Physics)*, *107*(A8), 1164. https://doi.org/10.1029/2001JA000278

Titov, V. S., Priest, E. R., & Demoulin, P. (1993). Conditions for the appearance of “bald patches” at the solar surface. *Astronomy & Astrophysics*, *276*, 564.

Wheatland, M. S., Sturrock, P. A., & Roumeliotis, G. (2000). An optimization approach to reconstructing force-free fields. *The Astrophysical Journal*, *540*(2), 1150–1155. https://doi.org/10.1086/309355